Title

A turbulence modeling study of the precessing vortex core in a pipe flow

Authors

Reis, Patrick
Younis, Bassam A
Weigand, Bernhard

Publication Date

2023-04-01

DOI

10.1016/j.ces.2023.118497

Chemical Engineering Science 269 (2023) 118497

Contents lists available at ScienceDirect

Chemical Engineering Science

journal homepage: www.elsevier.com/locate/ces

A turbulence modeling study of the precessing vortex core in a pipe flow

Patrick Reis [a], Bassam A. Younis [b,*], Bernhard Weigand [a]

[a] Institut für Thermodynamik der Luft- und Raumfahrt, Universität Stuttgart, 70569 Stuttgart, Germany
[b] Department of Civil & Environmental Engineering, University of California, Davis, CA 95616, USA

HIGHLIGHTS

- The phenomenon of precessing vortex core (PVC) is investigated computationally.
- Turbulence closure was with four alternative Reynolds-stress transport models.
- Good agreement obtained with experimental data for turbulent swirling flow in pipe.
- The simulations correctly capture self-sustained oscillations in bulk parameters.
- Flow visualizations reveal exceptionally well-defined double helical vortex.

GRAPHICAL ABSTRACT

ARTICLE INFO

Article history:
Received 31 October 2022
Received in revised form 9 January 2023
Accepted 16 January 2023
Available online 21 January 2023

Keywords:
Precessing vortex core
Reynolds-stress closures
Pressure-strain models

ABSTRACT

The phenomenon of precessing vortex core is observed experimentally when swirl is imparted on an axial flow in a pipe. It manifests as a coherent structure in the form of a helical vortex of regular wavelength whose axis is coincident with the pipe's axis. The most striking consequence of this pattern of flow is the generation of periodic fluctuations in the streamwise distribution of the wall static pressure and skin friction. While the prediction of the precessing vortex has proved possible with large-eddy simulations, there is no record of this phenomenon being captured in great detail by Reynolds-averaged Navier-Stokes methods utilizing turbulence models to close the time-averaged equations. The purpose of the research reported here was to determine whether the precessing vortex core and its impact on conditions at the wall can be captured using this approach. The turbulence model used was of the Reynolds-stress transport type which involves the solution of a differential transport equation for each of the six non-zero components of the Reynolds stress tensor. Previous studies in which such models were used in the prediction of rotating and swirling flows have shown that their performance is largely determined by the way in which the difficult fluctuating pressure-strain correlations that appear in these equations are modeled. To this end, four very different alternative models for these correlations were assessed by comparisons with experimental data for a swirling pipe flow at relatively high swirl number. It was found that the models do indeed capture the precessing vortex revealing it to be in the form of an exceptionally well-defined double vortex. It was also found that the expected periodic fluctuations in static pressure and wall skin friction, not previously obtained in turbulence model studies, are captured by the present closures.

* Corresponding author.
E-mail address: bayounis@ucdavis.edu (B.A. Younis).

https://doi.org/10.1016/j.ces.2023.118497
0009-2509/

Nomenclature

b_{ij}	Anisotropy tensor ($=\frac{\overline{u_iu_j}}{u_qu_q}-\frac{1}{3}\delta_{ij}$)
C_1,C_2, ...	Turbulence model coefficients
C_f	Wall friction coefficient ($=\frac{\tau_w}{0.5\rho U_b^2}$)
$C_{p,m}$	Pressure coefficient at centerline ($=\frac{p-p_{ref}}{0.5\rho U_b^2}$)
D	Pipe diameter
D_{ij}	Turbulence model parameter
D_h	Hydraulic diameter
f	Wall damping function
II_b	Second invariant of anisotropy ($=b_{ij}b_{ij}$)
k	Turbulence kinetic energy
L	Pipe length
$\mathscr{L}$	Turbulence length scale
P_{ij},P_k	Production rates of $\overline{u_iu_j}$ and k
p	Static pressure
Re	Reynolds number ($=\frac{U_bD}{\nu}$)
R_{ij}, $R_{\theta,ij}$	Reynolds-stress matrix in Cartesian and cylindrical-polar axes
S	Swirl number
S_{ij}	Mean rate of strain tensor
$T_{x,ij}$	Rotation matrix
U_i	Velocity vector
U	Axial velocity
$\overline{u_iu_j}$	Reynolds-stress tensor
W	Tangential velocity
W_{ij}	Mean vorticity tensor

Greek symbols

ε	Dissipation rate
ν	Kinematic viscosity
Φ_{ij}	Pressure-strain correlations
ρ	Density
θ	Angle in cylindrical-polar coordinates
τ	Shear stress
ζ	Distance normal to surface

Subscripts

b	Bulk
h	Hydraulic
ref	Reference
t	Turbulent
w	Wall

1. Introduction

This paper is concerned with the prediction of turbulent swirling flows in pipes in conditions leading to the formation of coherent structures that significantly modify the physical processes present. Swirling flows in general are of enormous interest due to their wide-spread occurrence in nature and in engineering practice such as in combustion systems (Syred, 2006), swirl chambers (Hedlund et al., 1999), cyclone separators (Murphy et al., 2007; Huard et al., 2010), vortex tubes for cyclone cooling (Seibold and Weigand, 2021), and thermal energy separation by swirl (Kobiela et al., 2018). They are also a class of flows where turbulence closures of the type used in engineering design have proved to be inadequate unless modified in some ad-hoc way (Kobayashi and Yoda, 1987; Chang and Chen, 1993; Gorbunova et al., 2016). In the flows of interest here, the imposition of a tangential component of velocity on the axial flow gives rise to an interesting phenomenon, namely the generation of a well-defined helical vortex that precesses around the tube's centerline. This feature is commonly referred to as a precessing vortex core (PVC). The vortex, whose direction of rotation is the same as that of the direction of the swirl at inlet to the pipe, is observed to occur when the swirl number (defined as the ratio of the tangential to axial momentum fluxes), and the axial Reynolds number are high. From a practical standpoint, the importance of this feature of the flow stems from the fact that it leads to the introduction of regular oscillations in the wall static pressure and in the skin friction that occur at a wave length that closely correlates with that of the precessing vortex (Cassidy and Falvey, 1970; Griffiths et al., 1998). Additionally, the peak-to-peak variations in the amplitudes of these parameters are observed to be quite large (Brar and Derksen, 2020). Unsteady pressure fluctuations can cause damage when they cause vibrations to occur especially at a frequency that coincides with the natural frequency of the pipe (Fick et al., 1996; Yoshida et al., 2009). Further, when heat and mass transfer processes are present (Khalatov and Shchukin, 2017), Reynolds analogy suggests that the precessing vortex will also cause oscillations to occur in the rates of heat and mass transfer from the walls leading perhaps to non-uniformity in distribution.

The literature on the computation and measurement of swirling flows is vast and a survey of it is well outside of the scope of this paper. Instead, we shall confine consideration to the case where swirl is introduced at inlet to the pipe by means of a swirl generator such as guide vanes, as opposed to the very different flow that arises when the pipe itself is rotated around its longitudinal axis. Consideration is further confined to cases where the flow is nominally axisymmetric, and where vortex breakdown, leading to the formation of the central recirculation zone, does not occur. Seibold et al. (2022) present a comprehensive review of flow and heat transfer in swirl tubes. Kitoh (1991), using hot-wire anemometry, obtained detailed measurements of the mean velocity components and the Reynolds stresses. These measurements revealed a number of features that directly point to the unsuitability of eddy-viscosity based turbulence closures in these flows. Among these features is the generation of very strong turbulence anisotropy due to the extra, swirl-related, rates of production of the Reynolds stresses. The accurate prediction of flows where turbulence anisotropy plays an important role in determining their behavior clearly points to the need to account for the normal stresses individually rather than by combining them into a single scalar parameter namely the turbulence kinetic energy. Another feature highlighted in Kitoh (1991) is the significant misalignment between the directions of the mean rates of strain and their associated turbulent stresses. This misalignment, which is a feature of all strongly-three-dimensional turbulent shear layers, is entirely due to history effects i.e. non-local effects that are produced by the advective and diffusive transport of the Reynolds stresses. It should be noted that Boussinesq's stress–strain relationship, which forms the basis of eddy-viscosity closures, enforces the alignment of these directions. It thus follows that the accurate prediction of swirling flows requires either the abandonment of eddy-viscosity closures altogether, or limiting their use merely to the representation of the small-scale dissipative motions that are less influential in defining the large-scale flow structures and their consequences. This is amply demonstrated in the study of Guo et al. (2002) who were the first to report on the prediction of turbulent vortex precession in a confined flow with swirl. Their particular application involved a flow in a pipe with an axisymmetric sudden expansion.

Three-dimensional, time-dependent calculations were performed with the effects of turbulence accounted for using the very large eddy simulations (VLES) approach to capture the large-scale flow structures, and the standard $k-\varepsilon$ model to represent the small-scale dissipative motions. The combination of performing the calculations in three-dimensional time-dependent mode and the reduced reliance on the standard eddy-viscosity model that results from the VLES approach enabled the capture of a very well defined precessing vortex core leading to self-sustaining oscillations in mean velocity and pressure. Li and Tomita (1994) reported measurements of mean velocities and the wall static pressure distribution for various values of the swirl number. No measurements of turbulence parameters were obtained, the focus being on the development of empirical correlations for the streamwise decay of the swirling motion. An important outcome of this study is the finding that the swirl number, which is constant in swirling jets that develop remotely from a solid wall, decays as flow develops along the pipe's length. This will be shown below to also occur in the present computations. Rocklage-Marliani et al. (2003) used three-dimensional laser-Doppler velocimetry to obtain detailed measurements of the mean flow and the Reynolds stresses in swirling pipe flow at reasonably high Reynolds number ($Re = 280,000$), and over a wide range of swirl numbers in which the main features of a precessing vortex core (referred to by the authors as' helically wound streamlines') were clearly displayed. The data from this study will be the focus of the present work. Escue and Cui (2010) reported on the prediction of this benchmark flow using two distinctly different turbulence model: the RNG $k-\varepsilon$ model, and a Reynolds-stress transport closure. In contrast to all previous predictions of swirling flows, it was found that the eddy-viscosity model generally performed better than the stress transport closure. No explanation was provided for this result, and neither model succeeded in producing the precessing vortex core or its effects on the wall shear stress and static pressure.

In this work, we have focused on Reynolds-stress transport closures in the knowledge that prediction of the precessing vortex core and its consequences will only be possible by properly accounting for the effects of turbulence anisotropy, and by allowing for the'history' effects leading to the non-alignment of the directions of turbulent stresses and mean rates of strain. Previous predictions of swirling flows with Reynolds-stress closures have all indicated that of all the assumptions made to approximate the unknown terms in the Reynolds-stress equations, the one that has the greatest bearing on the outcome is the choice of a model for the fluctuating pressure-strain rate correlations. Accordingly, we focus here on assessment of four alternative models for these terms that are quite different in their formulation. Thus, for example, two of the models require the inclusion of'wall damping' functions while the other two do away with these functions and yet produce the correct near-wall behavior. Other differences are discussed below - the objective being to determine whether different modeling assumptions lead to distinctly different predictions.

2. Mathematical formulation

The equations for conservation of mass and momentum for an incompressible flow with constant fluid properties are:

$$\frac{\partial U_i}{\partial x_i} = 0, \tag{1}$$

$$\frac{\partial U_i}{\partial t} + U_j \frac{\partial U_i}{\partial x_j} = \frac{\partial}{\partial x_j}\left(\nu\left(\frac{\partial U_i}{\partial x_j} + \frac{\partial U_j}{\partial x_i}\right) - \overline{u_i u_j}\right) - \frac{1}{\rho}\frac{\partial p}{\partial x_i}. \tag{2}$$

The unknown Reynolds stresses in Eq. (2) are obtained from the solution of differential transport equations for these quantities. These equations are of the form:

$$\overbrace{\frac{\partial \overline{u_i u_j}}{\partial t} + U_k \frac{\partial \overline{u_i u_j}}{\partial x_k}}^{Convection:C_{ij}} = \overbrace{-\left(\overline{u_i u_k}\frac{\partial U_j}{\partial x_k} + \overline{u_j u_k}\frac{\partial U_i}{\partial x_k}\right)}^{Production:P_{ij}} \overbrace{-\frac{\partial}{\partial x_k}\left[\overline{u_i u_j u_k} + \frac{1}{\rho}\left(\overline{p' u_i}\,\delta_{jk} + \overline{p' u_j}\,\delta_{ik}\right) - \nu\frac{\partial \overline{u_i u_j}}{\partial x_k}\right]}^{Diffusion:D_{ij}} + \overbrace{\frac{\overline{p'}}{\rho}\left(\frac{\partial \overline{u_i}}{\partial x_j} + \frac{\partial \overline{u_j}}{\partial x_i}\right)}^{Redistribution:\Phi_{ij}} - \overbrace{2\nu\left(\frac{\partial \overline{u_i}}{\partial x_k}\frac{\partial \overline{u_j}}{\partial x_k}\right)}^{Dissipation:\varepsilon_{ij}} \tag{3}$$

In the above, P_{ij} is the rate of production term which is exact and in no need of modeling. The diffusion term consists of three terms, namely turbulence fluctuations, pressure fluctuations and molecular diffusion of which only the latter is exact. In this work, the pressure diffusion term is neglected since the consensus of data suggests that it makes negligible contribution to the stress balances. The turbulent diffusion term is modeled as proposed by Daly and Harlow (1970) i.e. by assuming that the diffusion of a component of the Reynolds stress tensor is proportional to its spatial gradient:

$$-\overline{u_i u_j u_k} = C_s \frac{k}{\varepsilon}\overline{u_k u_l}\frac{\partial \overline{u_i u_j}}{\partial x_l} \tag{4}$$

The coefficient C_s is assigned its usual value of0.22.

The focus here is on the modeling of the fluctuating pressure-strain correlationsΦ_{ij}. The role of the pressure-strain correlations term (Φ_{ij}) is to redistribute the turbulence energy amongst the three normal-stress components and to reduce the shear stresses. It is therefore the most direct agency through which the turbulence anisotropy can be reproduced. The literature contains several proposals for modeling this term. For the purpose of determining their performance in this flow, we have chosen four of these models that each provides a distinctive feature that is absent in the others. In two of the models, Φ_{ij} is presented as the sum of three terms that account, respectively, for purely turbulent fluctuations ($\Phi_{ij,1}$), for interactions between the turbulent fluctuations and the mean rates of strain ($\Phi_{ij,2}$), and for corrections on these two terms to account for the effects of a solid wall on damping the pressure field in its vicinity ($\Phi_{ij,w}$):

$$\Phi_{ij} = \Phi_{ij,1} + \Phi_{ij,2} + \Phi_{ij,w} \tag{5}$$

The $\Phi_{ij,1}$ term is invariably modeled after Rotta's (1951) return-to-isotropy proposal:

$$\Phi_{ij,1} = -C_1\frac{\varepsilon}{k}\left(\overline{u_i u_j} - \frac{2}{3}\delta_{ij}k\right) \tag{6}$$

A model for the $\Phi_{ij,2}$ term was proposed by Launder et al. (1975) and can be written as:

$$\Phi_{ij,2} = \frac{(C_2+8)}{11}\left(P_{ij} - \frac{2}{3}\delta_{ij}P\right) - \frac{(8C_2-2)}{11}\left(D_{ij} - \frac{2}{3}\delta_{ij}P_{ij}\right) - \frac{(30C_2-2)}{55}k\left(\frac{\partial U_i}{\partial x_j} + \frac{\partial U_j}{\partial x_i}\right), \tag{7}$$

with

$$D_{ij} = \overline{u_i u_k}\frac{\partial U_k}{\partial x_j} + \overline{u_j u_k}\frac{\partial U_k}{\partial x_i}. \tag{8}$$

There are very few recorded instances where this model has been shown to produce results that are of accuracy commensurate with its complexity. In contrast, a truncated version of Eq. (7) has

proved to be very successful in a wide range of flows and is therefore selected for the present study. It is given by:

$$\Phi_{ij,2} = -C_2\left(P_{ij} - \frac{2}{3}\delta_{ij}P_{ij}\right). \tag{9}$$

The wall correction term $\Phi_{ij,w}$ is given by Gibson and Launder (1978) as:

$$\Phi_{ij,w} = \left\{C_1'\frac{k}{\varepsilon}\left(\bar{u_i u_j} - \frac{2}{3}\delta_{ij}\right) + C_2'\left(P_{ij} - k_{ij}\right)\right\}f \tag{10}$$

where f is the wall damping function:

$$f = C_w\frac{k^{3/2}/\varepsilon}{\zeta} \tag{11}$$

where k is the turbulent kinetic energy obtained as half the sum of the normal stresses, C_w is a scaling factor that sets the value of f to unity at the nearest wall cells, and ζ is the normal distance to the nearest wall.

The values assigned to the various coefficients in the above are listed in Table 1. In that table, the designation LRR indicates that the model coefficients are assigned the values suggested in Launder et al. (1975) and Gibson and Launder (1978). This model has given good results in a variety of flows but has proved unsatisfactory in the prediction of a flow that is directly relevant to the present study, namely that of the free axisymmetric swirling jet. Launder and Morse (1979), in a computational and experimental study of this flow, reported that, contrary to the measurements, the model predicted a spreading rate of the swirling jet that was lower than that of the equivalent non-swirling jet. The cause for this erroneous result was traced by Gibson and Younis (1986 a) to the weighting given to the terms in the pressure-strain models and an alternative set of coefficients was proposed that was found to yield much improved results for a variety of complex shear flows including that of the free swirling jet. In a later study of turbulent boundary layers developing over axially-rotated circular cylinders, Gibson and Younis (1986b) extended their model to account for wall-damping effects. This model is designated in Table 1 as GY.

In another group of models for the pressure-strain correlations, Φ_{ij} is modeled via the use of tensor representation theorems to represent it, a second-order tensor, in terms of combinations of first- and second-order tensors. The wall damping effects are not accounted for explicitly as with Eq. (10) but, rather, by adopting suitable weightings for the various terms in their formulation. Several models of this type have been proposed and used to varying degrees of success. They mostly can be expressed in a unified form as:

$$\begin{aligned}\Phi_{ij} = &-\left(C_1\varepsilon + C_1^* P_k\right)b_{ij} + C_2\varepsilon\left(b_{ik}b_{kj} - \tfrac{1}{3}b_{kl}b_{kl}\delta_{ij}\right)\\ &+\left(C_3 - C_3^* II_b^{\frac{1}{2}}\right)kS_{ij}\\ &+C_4k\left(b_{ik}S_{jk} + b_{jk}S_{ik} - \tfrac{2}{3}b_{kl}S_{kl}\delta_{ij}\right)\\ &+C_5k\left(b_{ik}W_{jk} + b_{jk}W_{ik}\right)\end{aligned} \tag{12}$$

In the above, b_{ij} $(=\bar{u_i u_j}/\bar{u_q u_q} - \frac{1}{3}\delta_{ij})$ is the turbulence anisotropy, II_b $(=b_{ij}b_{ij})$ is the second invariant of anisotropy, and W_{ij} $\left(=\frac{1}{2}\left(\frac{\partial U_i}{\partial x_j} - \frac{\partial U_j}{\partial x_i}\right)\right)$ is the mean vorticity tensor.

Different models can be obtained from Eq. (12) by assigning values to the coefficients that can be deduced by reference to data from homogeneous and inhomogeneous shear flows. Here, we choose two such models. The first is that of Speziale et al. (1991) (hereafter referred to as SSG) - a model that has found widespread application in a variety of flows including in those with swirl (Younis et al., 1996). The second is a model that differs from SSG in two important aspects: the term that is quadratic in the Reynolds stresses has been excluded on the basis that its presence is not supported by data on return to isotropy. Also excluded are the vorticity terms on the basis that their inclusion renders the model results dependent on the frame of reference chosen to perform the calculations (Dafalias and Younis, 2007, 2009). This model will hereafter referred to as DY. The coefficients assigned to the SSG and DY models are listed in Table 2.

The last term in Eq. (3) ε_{ij} is the rate of dissipation of $\bar{u_i u_j}$ by viscous action. At high turbulence Reynolds numbers, this term is modeled by assuming that at high turbulence Reynolds numbers, viscous dissipation is isotropic thus:

$$\varepsilon_{ij} = \frac{2}{3}\delta_{ij}\varepsilon, \tag{13}$$

where ε is the rate of dissipation of the turbulence kinetic energy k which is obtained from:

$$\frac{\partial\varepsilon}{\partial t} + U_i\frac{\partial\varepsilon}{\partial x_i} = \frac{\partial}{\partial x_i}\left(C_\varepsilon\frac{k}{\varepsilon}\bar{u_k u_i}\frac{\partial\varepsilon}{\partial x_i}\right) + C_{\varepsilon_1}\frac{\varepsilon}{k}P_k - C_{\varepsilon_2}\frac{\varepsilon^2}{k} \tag{14}$$

where the coefficients have been assigned their standard values (Tables 1 and 2).

3. Computational details

The experimental data used in this study are those of Rocklage-Marliani et al. (2003) obtained in a circular pipe with diameter $D = 0.1m$ and length of$L = 1.5m$. The bulk velocity was $U_b = 2.8$ m/s and the Reynolds number was$Re = 280,000$. Measurements of mean velocities and Reynolds stresses were obtained using laser-Doppler velocimetery and are reported at 5 axial locations in the region$4 \le x/D \le 14$.

A swirl generator, consisting of a rotating bundle of small tubes, was used to impose swirl on the axial flow. The strength of swirl is quantified by the swirl number (S) which represents the ratio of the tangential to axial momentum fluxes:

$$S = \frac{\int rWU\,dA}{D_h\int U^2\,dA}, \tag{15}$$

where D_h is the hydraulic diameter. In the present experiment, the initial swirl number was$S = 0.61$.

The computations were performed using OpenFOAM - an open source software tool for computational fluid dynamics (OpenFOAM, 2018). It utilizes finite-volume discretization to solve the equations governing the conservation of mass, momentum and the turbulence parameters which here consisted of all six non-zero components of the Reynolds-stress tensor, and the energy dissipation rate. The dependent variables are co-located at the cells center, and are solved iteratively using a segregated approach. The coupling between the continuity and momentum equations is achieved using the SIMPLE algorithm. Discretization was with second-order accurate schemes. For the advection terms, the bounded Gauss-limited linear scheme was used. This scheme,

Table 1
Coefficients for the LRR and GY models.

Model	C_1	C_2	C_1'	C_2'	$C_{\varepsilon 1}$	$C_{\varepsilon 2}$	C_ε
LRR	1.8	0.6	0.5	0.3	1.45	1.90	0.18
GY	3.0	0.3	0.75	0.5	1.40	1.80	0.15

Table 2
Coefficients for the SSG and DY models.

Model	C_1	C_1^*	C_2	C_3	C_3^*	C_4	C_5	$C_{\varepsilon 1}$	$C_{\varepsilon 2}$	C_ε
DY	4.0	3.0	0	0.8	2.0	0.6	0	1.45	1.9	0.18
SSG	3.41	1.8	4.2	0.8	1.31	1.25	0.41	1.44	1.83	0.18

which utilizes central differencing to interpolate values from the cell center to the centers of its faces, is recommended for the simulation of incompressible flows as it is formulated to promote the solutions boundedness and convergence (OpenFOAM, 2018). The diffusion terms were discretized using the Gauss linear unbounded scheme whereas the vector quantities were discretized using the V-limiter scheme. To maintain numerical stability, underrelaxation was used in the solution of the governing equations with typical values being 0.2 for the pressure and 0.5 for all the remaining dependent variables. To expedite convergence and to avoid instabilities arising from incompatible initial conditions, the computations were started with the $k-\varepsilon$ model and proceeded until a converged flow field was obtained before switching over to the Reynolds-stress transport models. Thereafter, the computations were continued until the normalized sum of the absolute residuals for all the variables over the entire field dropped by at least three orders of magnitude from their initial value. The number of iterations required to achieve this degree of convergence depended on the pressure-strain model used and was of the order of 1000 iterations with typical simulation times being of the order of 5 h on two nodes on a central computing network. Each node consisted of two Intel E5-2630 v3 2.4 GHz CPUs each with 8 cores, 16 threads and 64 GB of RAM.

Fig. 1 displays the computational domain, the coordinate axes and the implemented boundary conditions. In order to be able to capture the precessing vortex, the computational domain covered the entire pipe cross-section using the block-structured grid shown in Fig. 2. The choice of a block-structured grid with a Cartesian mesh in the central region in preference of a cylindrical-polar mesh covering the entire cross-section was motivated by the need to avoid the excessive cell skewness around the centerline and the singularity there (Hernandez-Perez et al., 2011). This whole-section approach, which was also adopted in the swirling pipe flow computations of Guo et al. (2002), is different from what is normally done in flows that are nominally axisymmetric where the grid is two-dimensional and covers only a small sector of the full cross section on the basis that gradients of all dependent variables are zero in the azimuthal direction.

Solving for the entire cross section requires a special treatment of the boundary conditions applied at inlet to the domain. There, measured mean velocities and the Reynolds stress profiles are to be specified but these were obtained in the experiment along a single radial line on the basis that the flow can be treated as axisymmetric. In order to implement the measured profiles across the complete cross section, polynomial functions were used to fit the discrete data points to functions that expressed the measured variables as a function of the radius. The function for axial velocity was then used to specify this variable at all grid nodes. For the remaining variables, it was assumed that along the radial axis$r$, the cylindrical coordinates x, r, θ are coincident with the Cartesian coordinates, x, y, z respectively, that are used in OpenFOAM. The tangential velocity function $W(r)$ was decomposed into the corresponding components in the Cartesian $y-$ and $z-$ directions and assigned to each cell surface depending on the midpoint coordinates. Thus the velocity components in the Cartesian coordinate system U_y and U_z were calculated from:

$$U_y(y(r), z(r)) = -W(r) \cdot \sin\theta \tag{16}$$

$$U_z(y(r), z(r)) = W(r) \cdot \cos\theta \tag{17}$$

The Reynolds stresses were also assumed to be axisymmetric in the swirl coordinates and hence were specified across the entire inlet plane according to the tensor-transformation rule:

$$R_{\theta,ij} = T_{x,ij}\, R_{ij}\, T^T_{x,ij}. \tag{18}$$

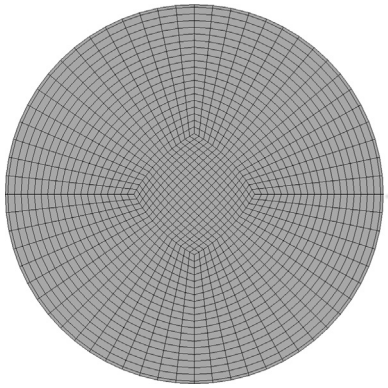

Fig. 2. Cross section of the grid used.

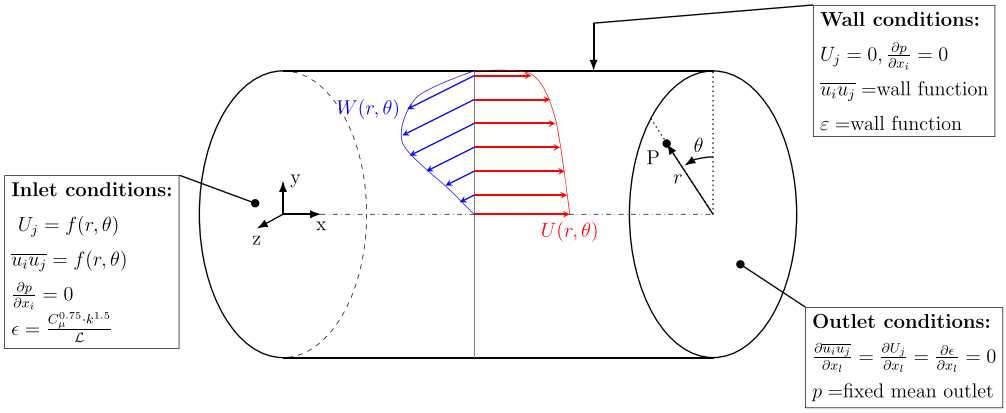

Fig. 1. Computational domain, coordinate axes and boundary conditions.

R_{ij} is the symmetric Reynolds stress matrix and $T_{x,ij}$ being the rotation matrix for a rotation θ around the x-axis. The superscript "T" denotes the transposed matrix.

$$T_{x,ij} = \begin{pmatrix} 1 & 0 & 0 \\ 0 & \cos\theta & -\sin\theta \\ 0 & \sin\theta & \cos\theta \end{pmatrix} \tag{19}$$

Also at the inlet plane, a zero axial gradient boundary condition was applied to the pressure while the dissipation rate was obtained from the relation:

$$\varepsilon = \frac{C^{0.75} \cdot k^{1.5}}{L} \tag{20}$$

where $C_\mu = 0.09$ and L is a length scale taken here to be$0.05D$.

The pipe walls were considered smooth and the boundary conditions there were specified based on conventional'wall function' approach. In this approach, the logarithmic law of the wall is used to obtain the resultant wall shear stress using the resultant velocity at the near-wall cells. The resultant stress was then resolved into axial and tangential components to provide the flux boundary conditions for the velocities in the respective directions. The normal gradient of each component of the Reynolds-stress tensor was set equal to zero while the value of ε at near-wall cells was set equal to the rate of energy production there. The location of the near-wall cells maintained in the range$30 < y^+ < 70$.

At pipe outlet, a fully-developed flow condition was assumed and hence the streamwise gradients of all variables except the pressure were set equal to zero. The pressure outlet boundary condition was set using the OpenFOAM option'fixedMeanOutletInlet'. With this option, the computed interior pressure field is extrapolated to the outlet plane using the near-cell values, and the distribution adjusted to satisfy overall continuity. In this way, the radial variation of pressure due to swirl, which is captured naturally in the interior cells, is correctly reflected at the outlet.

4. Results and discussion

A grid convergence study was conducted in order to quantify the discretization errors. Computations were thus performed on a coarse, medium and fine grids having$629,640$,$864,000$, and $1,132,560$ active grid nodes, respectively. The sensitivity of the computed solutions were assessed using the Grid Convergence Index (GCI) method (Roache, 1994; Celik et al., 2008) applied to three'target' parameters, namely the wall static pressure coefficient at inlet (C_p), the swirl number (S), and non-dimensionalized maximum axial velocity ($\widetilde{U}$), both evaluated at$x/D = 14$. The results of these tests are shown in Table 3. In that table, GCI^{21}_{fine} indicates the percentage the computed target parameter value is different from its asymptotic value. It is also an indication of the degree to which the solution would change with further grid refinement (Celik et al., 2008). For C_p and$\widetilde{U}$, the GCI is below 1% which indicates that the numerical errors are at a minimum. For$S$, the value is somewhat larger but that is typically obtained for parameters that are formed as a ratio of two computed quantities.

Also quoted in the table is the parameter Φ^{21}_{ext} which gives the asymptotic value of a particular target parameter as deduced by performing Richardson extrapolation. The convergence behavior is clearly illustrated in Fig. 3(a) and 3(b) which show the relation between the values of C_p and S as obtained with the three grids, and their asymptotic value. Notable in that figure is the drastic reduction in slope between the values obtained with the fine grid, and the asymptotic values indicating the attainment of satisfactory convergence with the fine grid which was therefore used in all subsequent computations. That mesh consisted of four blocks each $27 \times 22 \times 396$ nodes, and one center block with $22 \times 22 \times 396$ nodes in the radial, tangential and axial directions, respectively.

Fig. 4 compares the predicted and measured cross-stream profiles of the mean axial velocity at several axial locations. The profiles are non-dimensionalized with the bulk velocityU_b. The axial velocity profiles in Fig. 4 indicate the development of a region of momentum deficit at $r/D = 0.35$ which is obtained in both the measurements and the simulations. The *LRR* model shows an oscil-

Table 3
Grid convergence study.

	N_3	N_2	N_1	Φ_3	Φ_2	Φ_1	Φ^{21}_{ext}	e^{21}_a	e^{21}_{ext}	GCI^{21}_{fine}
C_p	629,640	864,000	1,132,560	1.178	1.169	1.166	1.163	0.306 %	0.235 %	0.292 %
S	629,640	864,000	1,132,560	0.483	0.489	0.493	0.507	0.831 %	2.66 %	3.42 %
$\widetilde{U}$	629,640	864,000	1,132,560	1.080	1.084	1.088	1.094	0.443 %	0.533 %	0.670 %

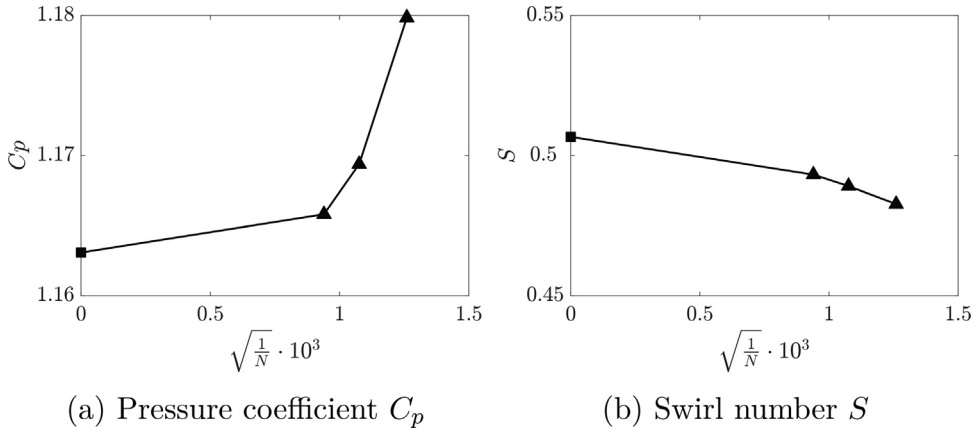

(a) Pressure coefficient C_p (b) Swirl number S

Fig. 3. Plot of the grid convergence analysis. ▲ solutions on the i^{th} grid, ■ asymptotic value from Richardson extrapolation.

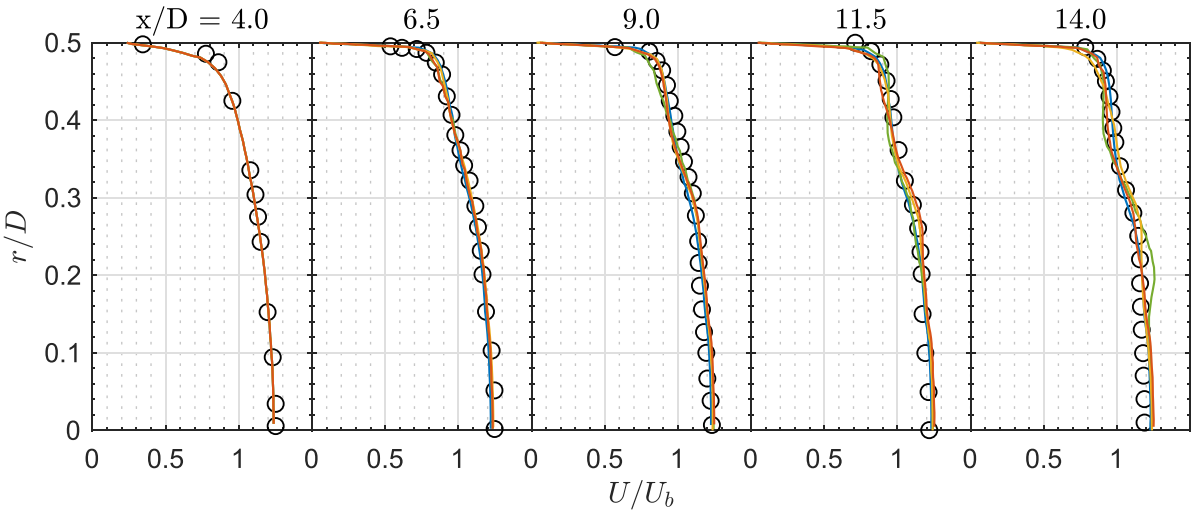

Fig. 4. Predicted and measured mean axial velocity at several streamwise locations. Predictions: (—) *GY*, (—) *LRR*, (—) *SSG*, (—) *DY*. Measurements (Rocklage-Marliani et al., 2003): °.

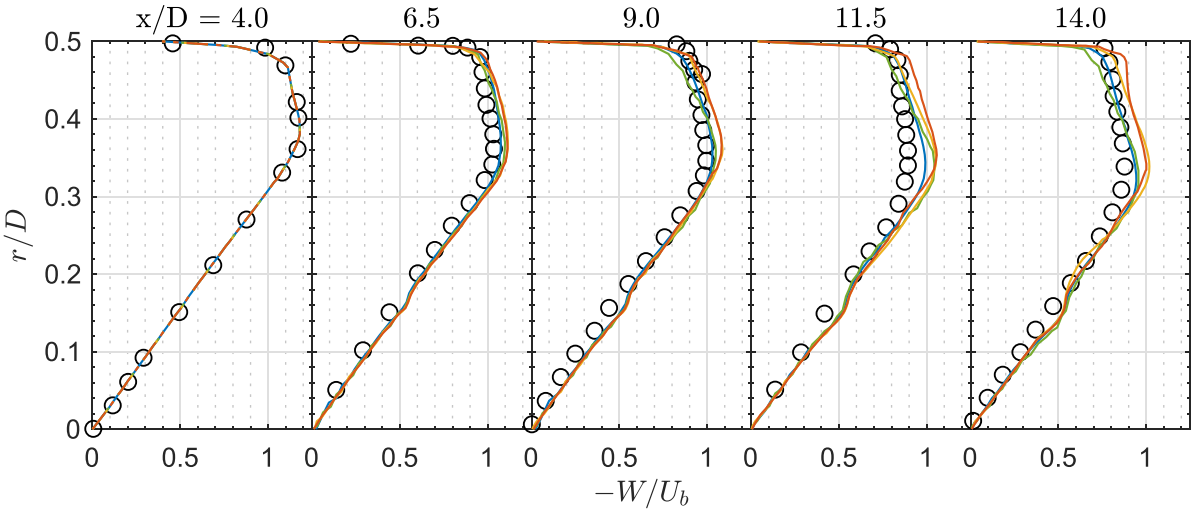

Fig. 5. Predicted and measured tangential velocity at several streamwise directions. Predictions: (—) *GY*, (—) *LRR*, (—) *SSG*, (—) *DY*. Measurements (Rocklage-Marliani et al., 2003): °.

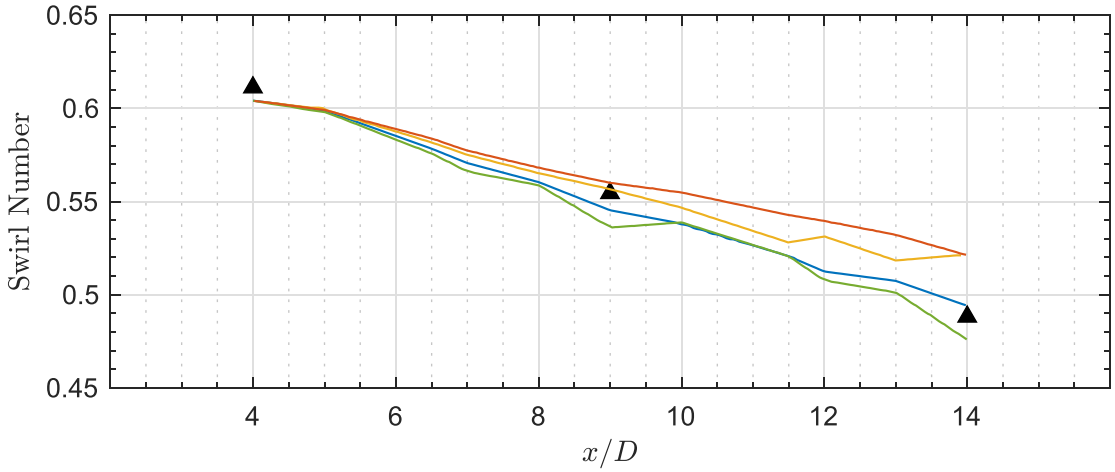

Fig. 6. Predicted and measured streamwise variation of the swirl number. Predictions: (—) *GY*, (—) *LRR*, (—) *SSG*, (—) *DY*. Measurements (Rocklage-Marliani et al., 2003): ▲.

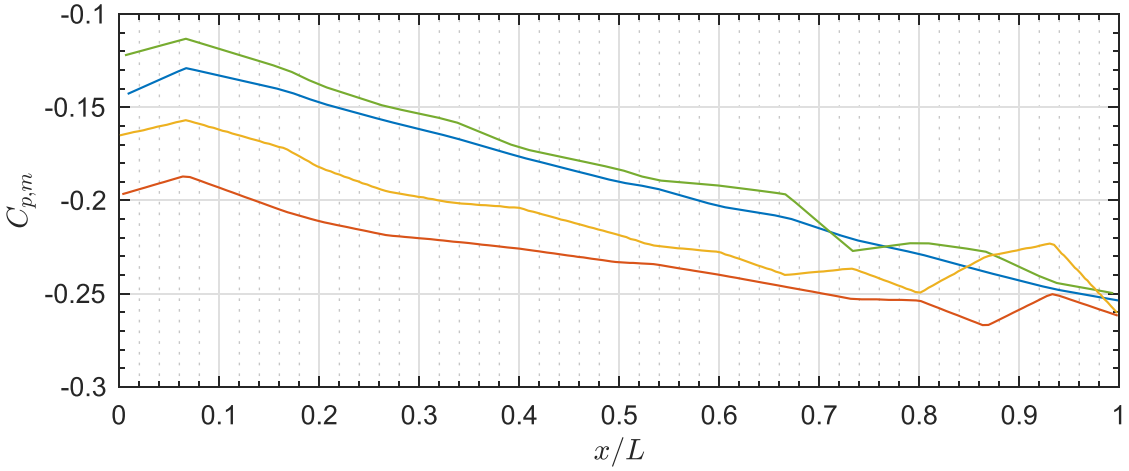

Fig. 7. Predicted streamwise variation of the centerline pressure coefficient. Predictions: (——) *GY*, (——) *LRR*, (——) *SSG*, (——) *DY*.

latory behavior which seems to exaggerate this deficit and compensate for it at $r/D = 0.2$ - a deficiency that becomes quite apparent at$x/D = 14.0$. The centerline velocity is predicted well with all the models though there appears to be a slight overestimation of this quantity close to the exit.

Fig. 5 compares the predicted and measured mean tangential velocity. In the inner region, the velocity profiles are essentially linear which implies characteristic of a forced vortex rotation which is to be expected since the swirl generator described by Rocklage-Marliani et al. (2003) imposes a forced vortex. Kitoh (1991) used tangential slots to generate the swirl, which, as in this flow, prevents the occurrence of centerline deflections due to the presence of guide vanes. In Kitoh (1991), the tangential profile is also categorized as zones of free (annular) and forced (central zone) vortex rotation in which the angles that the resultant velocity, the resultant velocity gradient and the resultant shear stress make with the axial direction are all different thus confirming the need for differential transport closures where these directions are not assumed to be coincident.

Rocklage-Marliani et al. (2003) report values for the swirl number at three streamwise locations. These are shown in Fig. 6 together with the models results. At inlet to the computational domain, the swirl number obtained using the measured gradients of U and W is somewhat lower than the measured value due to some minor deviations associated with the curve fitting the experimental profiles. As the flow develops, the swirl number decreases due to momentum loss at the walls by friction and this is obtained in both the measurements and the models. Close to the exit (at $x/D = 14$), some minor departures from the otherwise monotonic trend is observed in the results of *DY* and *SSG* which are the two models that do not explicitly account for the wall damping effects through a damping function.

The pressure drop that occurs in between inlet and exit is an important parameter to be quantified and minimized (El Sayed, 2015). Fig. 7 shows the predicted variation of the static pressure at the centerline along the streamwise direction. No experimental measurements are available for comparison. The differences in the models results are likely due to the different weighting given to the terms representing the turbulence-turbulence and the turbulence-mean rate of strain components of the models for the fluctuating pressure-strain correlations (Eq. (5)). These differences modify the mean velocities via the momentum diffusion terms and from there yield differences in the predicted mean pressure fields. The

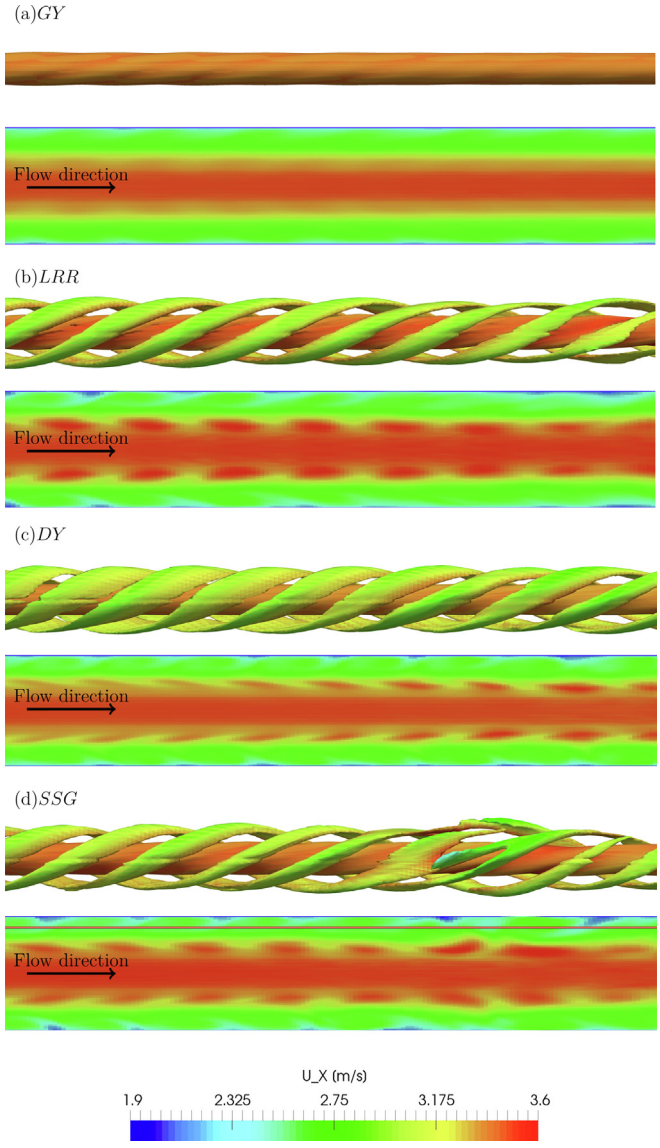

Fig. 8. Top for each model: vorticity isosurfaces for $\omega_x = -200/s$. Bottom for each model: contour plot of the axial velocity U_x at the centerline section.

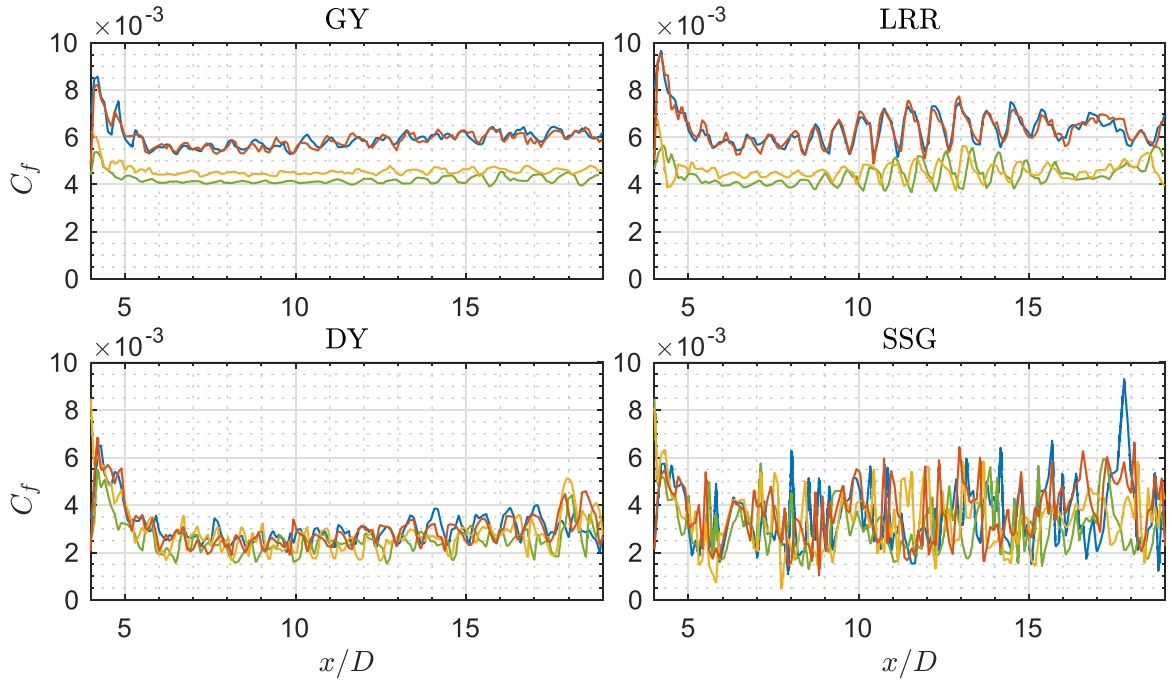

Fig. 9. Predicted streamwise variation of the wall-friction coefficient. Predictions: (——) $\theta = 0°$, (- - -) $\theta = 45°$, (- · -), $\theta = 67.5°$, (·····) $\theta = 90°$.

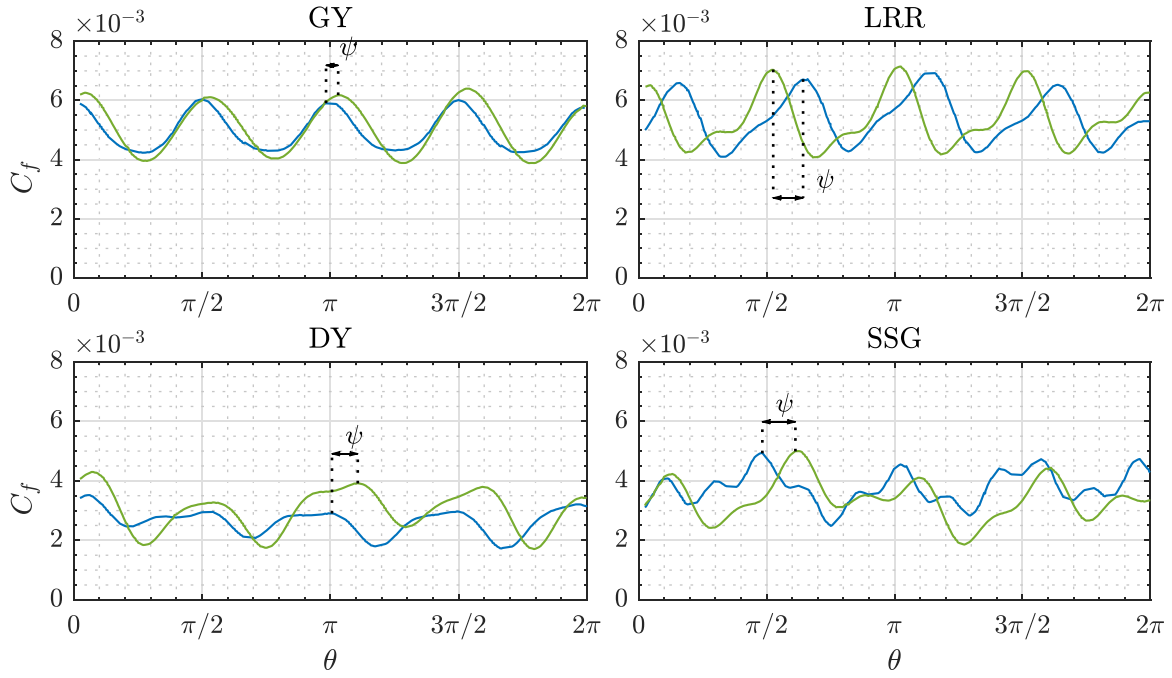

Fig. 10. Predicted variation of wall friction coefficient C_f with angular position θ at the two streamwise locations: $x/L = 0.633$ (- - -) and $x/L = 0.667$ (——).

initial rise in the pressure coefficient is due to the flow adjustment that inevitably occurs when the prescribed inlet conditions are not exactly matched, and because the radial component of velocity is set equal to zero for lack of data. In a non-swirling pipe flow at the same *Re* number, it would be anticipated that a decrease in the pressure coefficient of around $\Delta C_p \approx -0.2$ would occur over a similar distance (as suggested by the Darcy–Weisbach equation). This is what is approximately obtained here as well.

Having examined the profiles of the mean axial and tangential components of velocity at the limited number of streamwise locations where measurements are available, it is instructive to view the evolution of the flow field along the entire length of the pipe. This can conveniently be done by plotting contours of the isosurfaces of the axial component of vorticity ($\omega_x = \partial W/\partial y - \partial V/\partial z$)). These contours are presented in Fig. 8 for$\omega_x = -200/s$. Also plotted there are the contours of the axial velocity U_x at the middle section of the pipe$y = 0$. All the models show the expected vortex precession around the centerline, most strikingly by the models of*LRR*, *DY* and *SSG* that also show that the coherent structure is in the form of a double helix. This behavior is remarkably similar to the one

observed in the Delayed Detached Eddy Simulations (DDES) in a convergent vortex tube (Seibold and Weigand, 2021), and in the Direct Numerical Simulations (DNS) of swirling pipe flows of Vaidya et al. (2011) who suggested it to be analogous to that found in the Taylor-Couette flow that occurs between a stationary outer cylinder and a rotating inner one.

It was mentioned in the Introduction that an important feature of the Precessing Vortex Core is its effect on the processes that occur at the pipe's wall. The expected consequences of the helical structures that are apparent in Fig. 8 are that quantities that depend on the normal gradients of mean velocity will experience periodic fluctuations in the streamwise direction associated with the passage of peaks and troughs past a fixed point on the pipe's wall. This is clearly evident here in Fig. 9 where the streamwise variation of the wall friction coefficient C_f is plotted at four different angular positions within a quarter sector viz. at$\theta = 0^{\circ}$, 45°, 67.5°, and 90°. Several differences between the various models results are apparent. The *LRR* and *GY* models incorporate an explicit term to account for the wall damping effects and this is reflected in their results which show far less'noise' than is obtained with the *DY* and *SSG* models where these functions are absent. Concerning the overall behavior at a particular instant in time, it

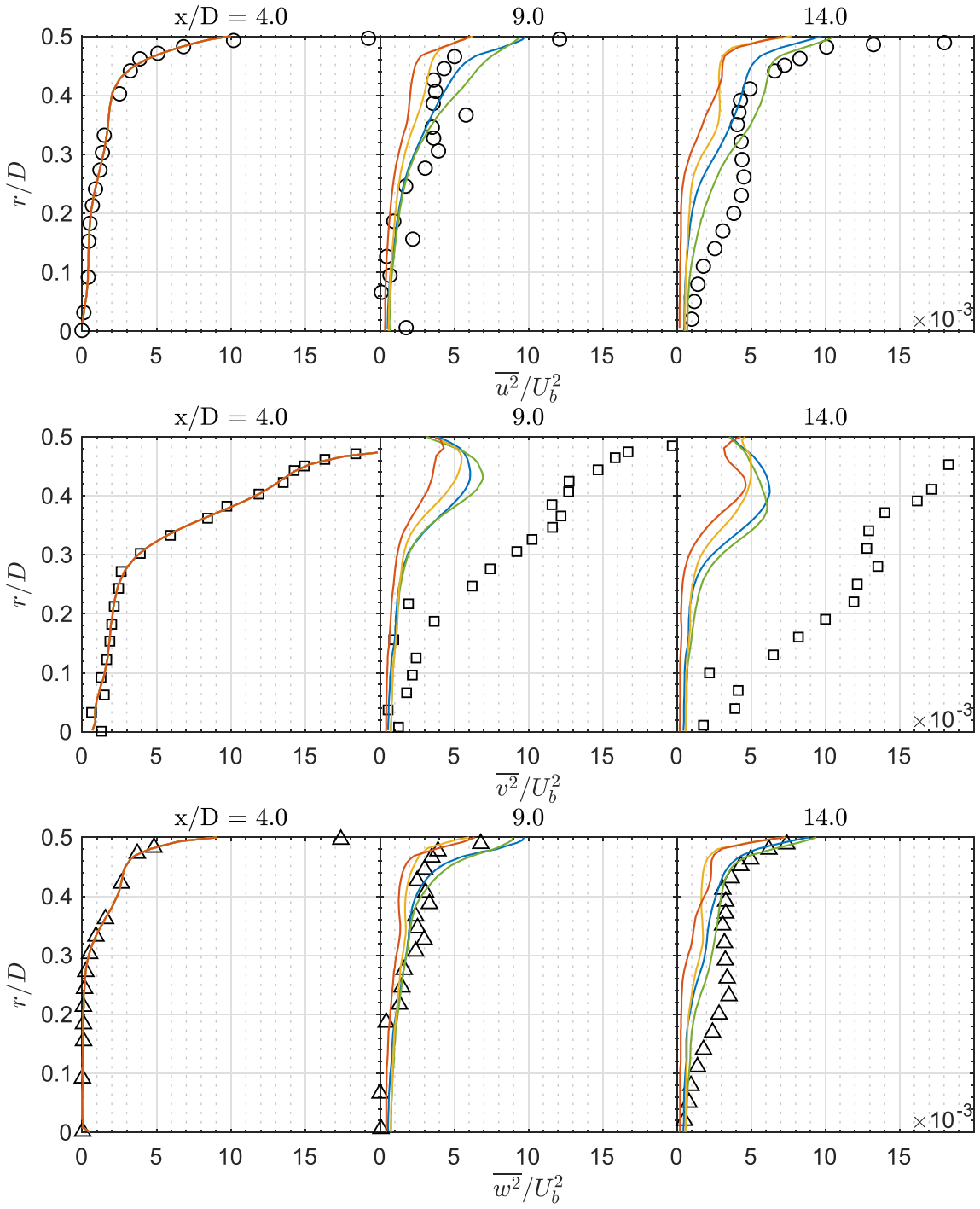

Fig. 11. Predicted and measured normal stresses at various streamwise sections. Predictions: (——) *GY*, (——) *LRR*, (——) *SSG*, (——) *DY*. Measurements (Rocklage-Marlian et al., 2003): u^2, v^2, Δw^2.

can be seen that the variations in the friction coefficient that occur for the two angular locations $\theta = 0^{\circ}$ and $\theta = 90^{\circ}$ are almost coincident, while the value of this coefficient is smallest at $\theta = 45^{\circ}$. By way of analogy, for a non-swirling flow in a pipe at the same Re, the wall-friction coefficient is somewhat lower at $C_f \approx 0.0036$.

The effects of the precessing vortex core on the circumferential distribution of the wall friction coefficient are expected to be periodic with significant variations between the peak and trough values. Fig. 10 show the variation of the wall friction coefficients with the angular position θ. The results are plotted at two streamwise locations viz. $x/L = 0.633$ and 0.667. A phase shift occurs at a roughly constant angle ψ. The phase shift is the least for the *GY* model.

Measurements of the Reynolds normal-stress components are reported at three sections ($x/D = 4, 9, 14$). The profiles are non-dimensionalized by the square of the bulk velocity U_b^2. The predicted and measured profiles are compared in Fig. 11 where the profiles prescribed at inlet are also plotted. The correspondence between predictions and measurements is quite satisfactory for the two normal-stress components $\bar{u}^2$ and $\bar{w}^2$ considering the possibility of some errors in the measurements which were obtained along a single radial line as opposed to the predictions which were averaged across the entire cross section. For the normal-stress component $\bar{v}^2$, the differences between predictions and measure-

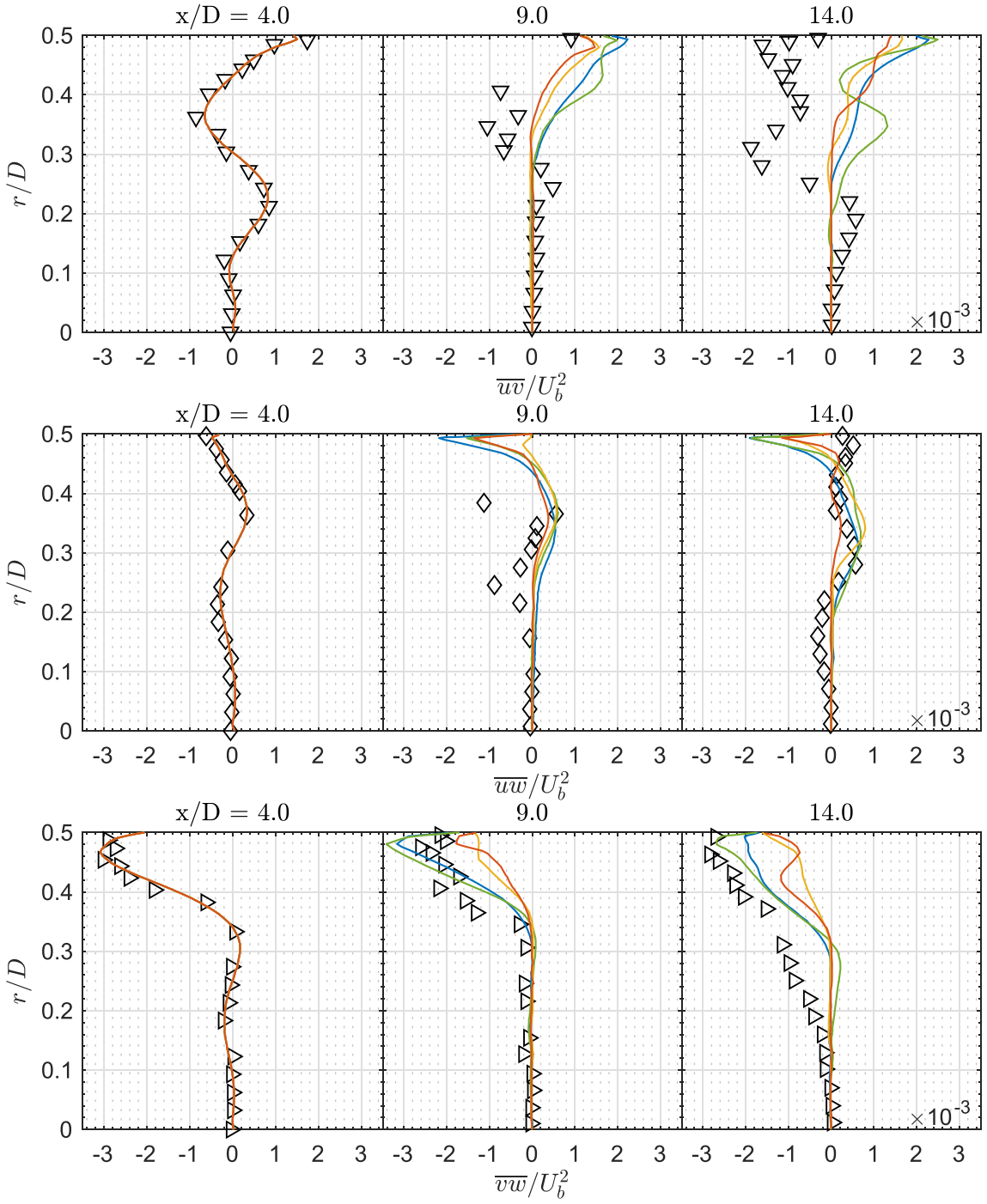

Fig. 12. Predicted and measured shear stresses at various streamwise locations. Predictions: (——) *GY*, (- - -) *LRR*, (·····) *SSG*, (-·-·-) *DY*. Measurements(Rocklage-Marlian et al., 2003): ∇ $\bar{u}\bar{v}$, $\bar{u}\bar{w}$, $\bar{v}\bar{w}$.

ments are very substantial with the latter showing very high levels of this stress component in the near-wall region that persist throughout the development length. At $x/D = 9.0$, for example, the level of $\bar{v^2}$ near the wall far exceeds that of $\bar{u^2}$ - a behavior that is not observed in any wall-bounded flow since the effects of a solid wall on the turbulence field is to dampen the fluctuations normal to it and redistribute the energy to the components parallel to the wall.

The predicted and measured profiles of the shear stresses are compared in Fig. 12. While there is broad consensus among the results obtained with the various models, significant differences with the measurements are apparent in the near-wall distribution of $\bar{uv}$ especially close to the outlet where the predicted and measured values are of opposite signs. In this regard, it should be noted that it is generally the case that the sign of $\bar{uv}$ is opposite that of $\partial U/\partial y$ and hence, according to the measurements of U presented in Fig. 4, the sign of the measured $\bar{uv}$ should be the same as in the predictions.

5. Concluding remarks

The aim of the work reported in this paper was to discover whether the interesting phenomenon of precessing vortex core as manifested by well-defined coherent structures can be captured by computational approaches that utilize turbulence models to close the Reynolds-averaged Navier-Stokes equations. Four turbulence models were selected, all being of the differential transport category, differing only in the way in which the fluctuating pressure-strain correlations are modeled. Two of the models utilized explicit functions to account for the wall-damping effects on the fluctuating pressure field, while two accounted for these effects indirectly through the weightings allocated to the various terms in their formulation. The purpose of performing the computations with four models was not to determine which performed'best' in these flows as it is very often the case that a model that yields the closest agreement with experiments with regards to one parameter does not do as well with regards to another. Rather, by obtaining results with four significantly different models, firmer conclusions can be arrived at regarding the degree of accuracy to which the PVC phenomenon can be predicted with Reynolds-averaged methods. Comparisons made with experimental measurements showed that all four models reproduce, to varying degrees of accuracy, the main features of the mean flow and the turbulence field with the noted exception of the vertical component of normal stresses. For that parameter, the measurements did not show the expected suppression of this quantity due to the stabilizing effects of solid-body rotation in contrast to the models which returned values that are consistent with expectations. On the other hand, the models were uniformly successful in capturing the structure of precessing vortex with the predicted contours of isovorticity showing that the coherent structures take on the form of a double helix rotating about the pipe's centerline. The consequences of this on processes that occur at the walls are quite profound and consisted of well-defined oscillations in static pressure and wall friction whose prediction has not hitherto been reported in the literature.

Having established in this study that the flow field due to this complex phenomenon can be predicted to acceptable engineering accuracy, it remains to be seen whether the prediction of scalar transport with its associated wall oscillations in the rates of heat or mass transport can also be achieved to the same degree of accuracy. Unlike in the mean-flow equations, where the contribution made by the pressure-gradient term to the momentum balance may mitigate deficiencies in modelling the turbulent transport terms, the equation for scalar transport contains no such agency and hence the greater emphasis on the accurate modeling of the turbulent scalar fluxes. There too it may well prove necessary to abandon eddy-viscosity based closures in favor of differential transport models for the turbulent scalar fluxes. Consideration of this matter is worthy of future research.

Data availability

Data will be made available on request.

Declaration of Competing Interest

The authors declare that they have no known competing financial interests or personal relationships that could have appeared to influence the work reported in this paper.

Acknowledgements

P. Reis gratefully acknowledges the financial support provided by the German academic exchange service (DAAD) and the Walter-Blohm-Stiftung that facilitated his stay at UC Davis.

References

Brar, L.S., Derksen, J.J., 2020. Revealing the details of vortex core precession in cyclones by means of large-eddy simulation. Chem. Eng. Res. and Design 159, 339–352.
Cassidy, J.J., Falvey, H.T., 1970. Observations of unsteady flow arising after vortex breakdown. J. Fluid Mech. 41, 727–736.
Celik, I.B., Ghia, U., Roache, P.J., 2008. Procedure for estimation and reporting of uncertainty due to discretization in CFD applications. J. Fluids Engg. 130, 078001.
Chang, K.C., Chen, C.S., 1993. Development of a hybrid $k-\varepsilon$ turbulence model for swirling recirculating flows under moderate to strong swirl intensities. Int. J. Num. Methods in Fluids 16, 421–443.
Dafalias, Y., Younis, B.A., 2007. Objective tensorial representation of the pressure-strain correlations of turbulence. Mechanics Research Communications 34, 319–327.
Dafalias, Y.F., Younis, B.A., 2009. Objective model for the fluctuating pressure-strain-rate correlations. J. Eng. Mech. 135, 1006–1014.
Daly, B.J., Harlow, F.H., 1970. Transport equations in turbulence. Phys Fluids 13, 2634–2649.
El Sayed, K., 2015. Optimization of the cyclone separator geometry for minimum pressure drop using Co-Kriging. Powder Technology 269, 409–424.
Escue, A., Cui, J., 2010. Comparison of turbulence models in simulating swirling pipe flows. Applied Mathematical Modelling 10, 2840–2849.
Fick, W., Syred, N., Griffiths, A.J., O'Doherty, T., 1996. Phase-averaged temperature characterized in swirl burners. Proc. Inst. Mech. Eng. Part A 210, 383–395.
Gibson, M.M., Launder, B.E., 1978. Ground effects on pressure fluctuations in the atmospheric boundary layer. J. Fluid Mech. 86, 491–511.
Gibson, M.M., Younis, B.A., 1986a. (a). Calculation of swirling jets with a Reynolds stress closure. Phys. Fluids 29, 38–48.
Gibson, M.M., Younis, B.A., 1986b. (b). Calculation of Boundary Layers With Sudden Transverse Strain. J. Fluids Engg. 108, 470–475.
Gorbunova, A., Klimov, A., Molevich, N., Moralev, I., Porfiriev, D., Sugak, S., Zavershinskii, I., 2016. Precessing vortex core in a swirling wake with heat release. Int. J. Heat Fluid Flow 59, 100–108.
Griffiths, A.J., Yazdabadi, P.A., Syred, N., 1998. Alternative eddy shedding set up by the non-axisymmetric recirculation zone at the exhaust of a cyclone dust separator. J. Fluids Eng. 120, 193–199.
Guo, B., Langish, T.A., Fletcher, D.F., 2002. CFD simulation of precession in sudden pipe expansion flows with inlet swirl. Applied Mathematical Modelling 26, 1–15.
Hedlund, C.R., Ligrani, P.M., Glezer, B., Moon, H.-K., 1999. Heat transfer in a swirl chamber at different temperature ratios and Reynolds numbers. Int. J. Heat Mass Transfer 42, 4081–4091.
Hernandez-Perez, V., Abdulkadir, M., Azzopardi, B.J., 2011. Grid generation issues in the CFD modelling of two-phase flow in a pipe. J. Comp. Multiphase Flows 3, 13–26.
Huard, M., Briens, C., Berruti, F., Gauthier, T.A., 2010. A Review of Rapid Gas-Solid Separation Techniques. Int. J. Chemical Reactor Engineering 8, 1–72.
Khalatov, A.A., Shchukin, V.K., 2017. Effect of flow swirl on local heat and mass transfer in turbulent flow in pipe inlets. Heat Transfer - Soviet Research 11, 10–15.
Kitoh, O., 1991. Experimental study of turbulent swirling flow in a straight pipe. J. Fluid Mech. 225, 445–479.
Kobayashi, T., Yoda, M., 1987. Modified k- ε model for turbulent swirling flows in a straight pipe. JSME Intl J. 30, 66.

Kobiela, B., Younis, B.A., Weigand, B., Neumann, O., 2018. A computational and experimental study of thermal energy separation by swirl. Int. J. Heat Mass Transfer 124, 11–19.

Launder, B. E., Morse, A. P., 1979. Numerical prediction of axisymmetric free shear flows with a Reynolds stress closure, Turbulent Shear Flows I, (eds. F. Durst, B. E. Launder, F. W. Schmidt, J. H. Whitelaw, Springer-Verlag Berlin Heidelberg), 279-285.

Launder, B.E., Reece, G.J., Rodi, W., 1975. Progress in the development of a Reynolds stress turbulence closure. J. Fluid Mech. 68, 537–566.

Li, H., Tomita, Y., 1994. Characteristics of swirling flow in a pipe. ASME J. Fluids Engg. 116, 370–373.

Murphy, S., Delfos, R., Pourquié, M.J., Olujic, Z., Jansens, P.J., Nieuwstadt, F.T.M., 2007. Prediction of strongly swirling flow within an axial hydrocyclone using two commercial CFD codes. Chem. Eng. Sci. 62, 1619–1635.

OpenFOAM, 2018. OpenFOAM v6 User Guide. https://doc.cfd.direct/openfoam/user-guide-v6/fvschemes (accessed 1/1/2023).

Roache, P.J., 1994. Perpective: A method for uniform reporting of grid refinement studies. J. Fluids Engg. 116, 405–413.

Rocklage-Marliani, G., Schmidts, M., Vasanta Ram, V.I., 2003. Three-dimensional laser-Doppler velocimeter measurements in swirling turbulent pipe flow. Flow, Turbulence and Combustion 1–4, 43–67.

Rotta, J.C., 1951. Statistische Theorie nichthomogener Turbulenz. Zeitschrift für Physik 129, 547–572.

Seibold, F., Weigand, B., 2021. Numerical analysis of the flow pattern in convergent vortex tubes for cyclone cooling applications. Int. J. Heat Fluid Flow 90, 1–16.

Seibold, F., Ligrani, P., Weigand, B., 2022. Flow and heat transfer in swirl tubes - A review. Int. J. Heat Mass Transfer 187, 1–26.

Speziale, C.G., Sarkar, S., Gatski, T.B., 1991. Modelling the pressure-strain correlation of turbulence: an invariant dynamical systems approach. J. Fluid Mech. 227, 245–272.

Syred, N., 2006. A review of oscillation mechanisms and the role of the precessing vortex core (PVC) in swirl combustion systems. Prog. Energy Combust. Sci. 32, 93–161.

Vaidya, H.A., Ertunç, O., Genc, B., Beyer, F., Koksoy, C., Delgado, A., 2011. Numerical simulations of swirling pipe flows- decay of swirl and occurrence of vortex structures. J. Phys.: Conf. Ser. 318.

Yoshida, H., Inada, Y., Fukui, K., Yamamoto, T., 2009. Improvement of gas-cyclone performance by use of local fluid flow control method. Powder Technology 193, 6–14.

Younis, B.A., Gatski, T.B., Speziale, C.G., 1996. Assessment of the SSG pressure-strain model in free turbulent jets with and without swirl. J. Fluids Engg. 118, 800–809.